

DSCC2010-(00'

CONNECTION VECTOR FIELDS AND OPTIMIZED COORDINATES FOR SWIMMING SYSTEMS AT LOW AND HIGH REYNOLDS NUMBERS

Ross L. Hatton*

Robotics Institute and
Department of Mechanical Engineering
Carnegie Mellon University
Pittsburgh, Pennsylvania 15232
rlhatton@cmu.edu

Howie Choset

Robotics Institute
Carnegie Mellon University
Pittsburgh, Pennsylvania 15232
choset@cmu.edu

ABSTRACT

Several efforts have recently been made to relate the displacement of swimming three-link systems over strokes to geometric quantities of the strokes. While this approach has been successful for finding net rotations, noncommutivity concerns have prevented it from working for net translations. Our recent results on other locomoting systems have shown that the degree of this noncommutivity is dependent on the coordinates used to describe the problem, and that it can be greatly mitigated by an optimal choice of coordinates. Here, we extend the benefits of this optimal-coordinate approach to the analysis of swimming at the extremes of low and high Reynolds numbers.

1 INTRODUCTION

Swimming has gained attention in fields ranging from fluid mechanics to biology. The physics of self-propulsion through a surrounding fluid have long driven new results in these areas and led to insightful observations regarding the behavior of swimming organisms [1–3]. A particularly interesting observation is that the optimal swimming motions for systems at both low and high Reynolds numbers are essentially the same, even though the fluid forces are dominated by viscous drag at low Reynolds numbers and by inertial accelerations at high Reynolds numbers [4].

Historically, swimming dynamics have been investigated by applying a stroke pattern (taken from nature or intuition) to a model of the swimming system and then analyzing the resulting forces and displacements. More recently, the strokes themselves have been the focus of attention, with optimal patterns found at low [5] and high [6] Reynolds numbers. While these

optimizations have primarily been achieved by parameterizing a stroke primitive and finding the parameters which give the best performance, a second research thrust has applied curvature techniques based on Lie brackets or curl to differential geometric formulations of the system models to directly find useful gaits [4, 7–9]. These curvature approaches successfully capture the net displacements resulting from infinitesimal strokes, but due to noncommutativity,¹ provide only the net rotations and coarse approximation of the net translations resulting from finite changes in shape.

The development of the geometric models for swimming has been paralleled by the development of similar models for non-holonomically constrained systems [10–14]; this line of research has included similar Lie bracket and curl approaches to those developed in the swimming community. The parallel developments are unsurprising, as both branches of inquiry are based on the same underlying body of theory, starting with [15]. Working within the context of nonholonomic mechanics, we have recently developed several mathematical tools for working with the geometric models. The first of these, the connection vector field [16], provides a visual representation of the kinematics of locomoting systems. Our second development, optimized coordinate choice [17, 18], reduces the noncommutativity of the systems and expands the benefit of the Lie bracket and curl techniques, providing close approximations of the net translations over finite strokes.

The primary goal of this paper is to demonstrate the applicability of these tools, particularly the coordinate optimization pro-

¹The net displacement over a trajectory depends on the order of intermediate translations and rotations, and the curvature techniques discard all or some of this ordering information.

*Address all correspondence to this author.

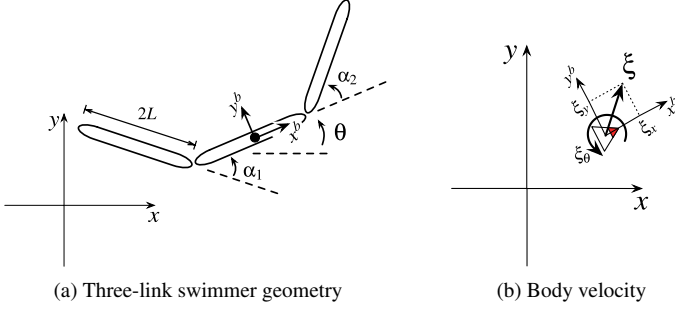


Figure 1: MODEL COORDINATES

cess, to swimming systems at low and high Reynolds numbers; this purpose is achieved in §§3-5. In §6, we then use these tools to examine the phenomena underlying previous numerical results for optimized swimming. Preparatory to this analysis, we use §2 to briefly review the previously developed geometric swimming models. Our intention in presenting these models is to provide an intuitive understanding of their derivation to a reader familiar with vector calculus but not differential geometry; accordingly, we have limited the presence of geometric terminology in the text and moved it into the footnotes. It is our hope that these notes will serve as a starting point for the reader who wishes to dig deeper into the literature on the underlying mathematical structures.

2 SYSTEM MODELS

In this paper, we analyze the motion of three-link systems of the form illustrated in Fig. 1(a), swimming at the extremes of low and high Reynolds numbers. This three-link model was proposed by Purcell [2] as the simplest system capable of swimming at low Reynolds numbers, and similar reasoning [6] suggests the use of this model for the high Reynolds number case. The motion of the swimmers as they interact with their surroundings is dictated by the *reconstruction equation*, which encodes constraint forces and momentum conservation rules as functions of the system shape and shape velocity. At both low and high Reynolds numbers, the reconstruction equation simplifies to a kinematic form, generated respectively from the drag forces on the swimmer or the net conservation of momentum between the swimmer and the surrounding fluid.

2.1 The Reconstruction Equation and the Local Connection

When analyzing a multi-body locomoting system, it is convenient to separate its configuration space Q (*i.e.* the space of its generalized coordinates q) into a position space G and a shape space M , such that the position $g \in G$ locates the system in the world, and the shape $r \in M$ gives the relative arrangements of its bodies.² For example, the position of the three-link system

²In the parlance of geometric mechanics, this assigns Q the structure of a (trivial, principle) *fiber bundle*, with G the *fiber space* and M the *base space*.

in Fig. 1(a) is the location and orientation of the middle link, $g = (x, y, \theta) \in SE(2)$,³ and its shape is parameterized by the two joint angles, $r = (\alpha_1, \alpha_2)$.

With this separation, locomotion is readily seen as the means by which changes in shape (such as strokes, gaits, or wing-beats) affect the position. The geometric mechanics community [11–14] has addressed this problem with the development of the *reconstruction equation* and the *local connection*, tools for relating the body velocity of the system, ξ , *i.e.* its longitudinal, lateral, and rotational velocity as depicted in Fig. 1(b), to its shape velocity \dot{r} , and accumulated momentum p .

The general reconstruction equation is of the form

$$\xi = -\mathbf{A}(r)\dot{r} + \mathbf{\Gamma}(r)p, \quad (1)$$

where $\mathbf{A}(r)$ is the *local connection*, a matrix which relates joint to body velocity, $\mathbf{\Gamma}(r)$ is the *momentum distribution function*, and p is the *generalized nonholonomic momentum*, which captures how much the system is “coasting” at any given time [12].

For systems that are sufficiently constrained or unconstrained, such as at the extremes of very low and very high Reynolds numbers, the generalized momentum drops out and the system behavior is dictated by the *kinematic reconstruction equation*,

$$\xi = -\mathbf{A}(r)\dot{r}, \quad (2)$$

in which the local connection thus acts as a kind of Jacobian, mapping from velocities in the shape space to the corresponding body velocity. For the rest of this paper, we will focus our attention on exploiting the structure of this kinematic reconstruction equation.

2.2 Low Reynolds Number Swimmer

At very low Reynolds numbers, viscous drag forces dominate the fluid dynamics of swimming and any inertial effects are immediately damped out. This effect has two consequences, which we can combine [4, 9] to express the equations of motion for this system in a kinematic reconstruction equation of the form in (2). First, the drag forces on the swimmer are linear functions of the body and shape velocities. Second, the net drag forces and moments on an isolated system interacting with the surrounding fluid go to zero.

For an illustration of the first consequence, consider a three-link swimmer with links modeled as slender members according to Cox theory [19]. For simplicity here, we regard the flows around each link as independent, per resistive force theory, but the solution for coupled flows is of the same form. The drag forces and moments on the i th link are based on a principle of lateral drag forces being approximately twice the longitudinal forces [19], with the moment around the center of the link found

³ $SE(2)$ is the set of all translations and rotations in the plane.

by assuming the lateral drag forces to be linearly distributed along the link according to its rotational velocity, *i.e.*,

$$F_{i,x} = \int_{-L}^L \frac{1}{2} k \xi_{i,x} d\ell = kL \xi_{i,x} \quad (3)$$

$$F_{i,y} = \int_{-L}^L k \xi_{i,y} d\ell = 2kL \xi_{i,y} \quad (4)$$

$$M_i = \int_{-L}^L k \ell (\ell \xi_{i,\theta}) d\ell = \frac{2}{3} kL^3 \xi_{i,\theta}, \quad (5)$$

where $F_{i,x}$ and $F_{i,y}$ are respectively the longitudinal and lateral forces, M_i the moment, k the differential viscous drag constant, and $\xi_i = [\xi_{i,x}, \xi_{i,y}, \xi_{i,\theta}]^T$ is the body velocity of the center of the i th link.⁴ The link body velocities are readily calculated from the system body and shape velocities as

$$\xi_1 = \begin{bmatrix} \cos(\alpha_1) \xi_x - \sin(\alpha_1) \xi_y + \sin(\alpha_1) L \dot{\xi}_\theta \\ \sin(\alpha_1) \xi_x + \cos(\alpha_1) \xi_y - (\cos(\alpha_1) + 1) L \dot{\xi}_\theta + L \dot{\alpha}_1 \\ \xi_\theta - \dot{\alpha}_1 \end{bmatrix} \quad (6)$$

$$\xi_2 = \xi \quad (7)$$

$$\xi_3 = \begin{bmatrix} \cos(\alpha_2) \xi_x + \sin(\alpha_2) \xi_y + \sin(\alpha_2) L \dot{\xi}_\theta \\ -\sin(\alpha_2) \xi_x + \cos(\alpha_2) \xi_y + (\cos(\alpha_2) + 1) L \dot{\xi}_\theta + L \dot{\alpha}_2 \\ \xi_\theta + \dot{\alpha}_2 \end{bmatrix}, \quad (8)$$

where the velocity of the second link is identified with the body velocity of the system, and all are clearly linear functions of ξ and $\dot{\alpha}$ and nonlinear functions of α . By extension, the forces in (3)–(5), which are linearly dependent on the link body velocities, are also linear functions of ξ and $\dot{\alpha}$ and nonlinear functions of α . Summing these forces into the net force and moment on the system (as measured in the system's body frame),

$$\begin{bmatrix} F_x \\ F_y \\ M \end{bmatrix} = \begin{bmatrix} \cos \alpha_1 & \sin \alpha_1 & 0 \\ -\sin \alpha_1 & \cos \alpha_1 & 0 \\ -L \sin \alpha_1 & -L(1 + \cos \alpha_1) & 1 \end{bmatrix} \begin{bmatrix} F_{1,x} \\ F_{1,y} \\ M_1 \end{bmatrix} + \begin{bmatrix} F_{2,x} \\ F_{2,y} \\ M_2 \end{bmatrix} + \begin{bmatrix} \cos \alpha_2 & -\sin \alpha_2 & 0 \\ \sin \alpha_2 & \cos \alpha_2 & 0 \\ L \sin \alpha_2 & L(1 + \cos \alpha_2) & 1 \end{bmatrix} \begin{bmatrix} F_{3,x} \\ F_{3,y} \\ M_3 \end{bmatrix}, \quad (9)$$

preserves the linear relationship with the velocity terms while only adding further nonlinear dependence on α , such that the net forces $F = [F_x, F_y, M]^T$ can be expressed with respect to the velocities as

$$F = \omega(\alpha) \begin{bmatrix} \xi \\ \dot{\alpha} \end{bmatrix}, \quad (10)$$

⁴Note that by "body velocity", we mean the longitudinal, lateral, and rotational velocity of the link, and not its velocity with respect to the body frame of the system.

where ω is a 3×5 matrix.

We now turn to the second consequence of being at low Reynolds number, that the net forces and moments on an isolated system should be zero, *i.e.* $F = [0, 0, 0]^T$. Applying this rule and separating ω into two sub-blocks gives

$$\begin{bmatrix} 0 \\ 0 \\ 0 \end{bmatrix} = [\omega_1^{3 \times 3} \quad \omega_2^{3 \times 2}] \begin{bmatrix} \xi \\ \dot{\alpha} \end{bmatrix}, \quad (11)$$

and thus $\omega_1 \xi = -\omega_2 \dot{\alpha}$ and

$$\xi = -\omega_1^{-1} \omega_2 \dot{\alpha}. \quad (12)$$

Finally, setting $\mathbf{A} = \omega_1^{-1} \omega_2$ puts (12) into the form of (2), with the viscous drag forces thus generating the local connection for the low Reynolds number system. In the hydrodynamically coupled case, the viscous flows around the links that produce the drag forces in (3)–(5) additionally depend on the relative positions and velocities of the links, but retain the linear relationships with ξ and $\dot{\alpha}$ that produce (10) and its sequels [4].

2.3 High Reynolds Number Swimmer

At very large Reynolds numbers, viscous drag is negligible and inertial effects dominate the swimming dynamics. While these conditions appear to be the direct opposite of those in the low Reynolds number case, they also result in the system equations of motion forming a kinematic reconstruction equation. This fact can be demonstrated via several approaches of varying technical depth [4, 8], but to maximize the physical intuition associated with this derivation, we give here a novel presentation based on the Lagrangian approach for the planar skater used in [13, 14].

The heart of this approach is the recognition that for a momentum-conserving system whose Lagrangian is equal to its kinetic energy (*i.e.* it has no means of storing potential energy), and whose kinetic energy can be expressed as

$$KE = \frac{1}{2} [\xi \quad \dot{r}] \mathbb{M}(r) \begin{bmatrix} \xi \\ \dot{r} \end{bmatrix}, \quad (13)$$

the mass matrix \mathbb{M} contains within itself the local connection. Specifically, \mathbb{M} is of the form

$$\mathbb{M} = \begin{bmatrix} \mathbb{I}(r) & \mathbb{I}(r) \mathbf{A}(r) \\ (\mathbb{I}(r) \mathbf{A}(r))^T & m(r) \end{bmatrix}, \quad (14)$$

from which \mathbf{A} is easily extracted.⁵

⁵In the works from which this derivation was inspired, $\mathbb{I}(r)$ appears as the

Given this relationship, it just remains to be shown that the three-link swimmer at high Reynolds number meets the aforementioned conditions. The first condition, that momentum is conserved in the system, follows from the lack of dissipative forces in the high Reynolds number regime. The second condition, that the Lagrangian equal the kinetic energy, can be easily seen by observing that for a planar system with no gravity effects in the plane, there is no mechanism for storing potential energy, leaving only the kinetic term in the Lagrangian. The third condition is more subtle, and as above, we will use a hydrodynamically decoupled example while noting the existence of an equivalent coupled solution.

An object immersed in a fluid displaces this fluid as it moves. In an ideal inviscid fluid, the drag forces on the object are entirely due to this displacement, and act as directional *added masses* \mathcal{M} on the object that sum with the actual inertia of the object to produce the effective inertia of the combined system. The added masses of single rigid bodies (and elements of articulated bodies when the inter-body fluid interactions are neglected) are solely functions of the geometries of the bodies. For example, the added mass tensor of an ellipse with semi-major axis a and semi-minor axis b in a fluid of density ρ is

$$\mathcal{M} = \begin{bmatrix} \mathcal{M}_x & 0 & 0 \\ 0 & \mathcal{M}_y & 0 \\ 0 & 0 & \mathcal{M}_\theta \end{bmatrix} = \begin{bmatrix} \rho\pi b^2 & 0 & 0 \\ 0 & \rho\pi a^2 & 0 \\ 0 & 0 & \rho(a^2 - b^2)^2 \end{bmatrix}, \quad (15)$$

with \mathcal{M}_x , \mathcal{M}_y , and \mathcal{M}_θ respectively corresponding to the added mass for longitudinal, lateral, and rotational motion.

Returning to the three-link swimmer, the kinetic energy associated with motion of the i th link through the fluid is

$$KE_i = \frac{1}{2} \xi_i^T (I_i + \mathcal{M}_i) \xi_i, \quad (16)$$

where I_i is the link's inertia tensor and ξ_i is its body velocity, as calculated in (6)–(8). Using the same linear dependence of ξ_i on ξ and \dot{r} as we exploited in the low Reynolds number case, it is relatively easy to transform (16), and thus $KE = \sum KE_i$, into the form of (13), and from there to extract the local connection \mathbf{A} . The derivation for the hydrodynamically coupled case is essentially similar, with the chief difference being the additional dependence of \mathcal{M} on r , which captures the distortion of the flow around each link caused by the proximity of the other links [4].

2.4 Similarity to Nonholonomic Systems

While the swimming systems described above appear very different from the nonholonomically constrained systems we

locked inertia tensor of an articulated body on a frictionless plane (*i.e.* its mass and rotational inertia with its joints locked in a given position). In the present fluid example, \mathbb{I} has a similar interpretation, except that its product with velocity produces the *impulse* of the combined fluid/rigid system rather than the momentum.

have examined in our previous work, there are some strong underlying similarities. The ω matrix for the low Reynolds number system in (11) acts as a *Pfaffian constraint* on the system, multiplying the body and shape velocities to produce a zero vector. This Pfaffian constraint form also appears in the case of systems with nonholonomic constraints, such as wheels that can roll but not slip sideways. In fact, with just two small changes, we can convert the low Reynolds number swimmer into the *three-link kinematic snake* [14, 17] which has a nonholonomic constraint (such as a passive wheelset) at the center of each link, preventing lateral motion but freely allowing longitudinal and rotational motion. First, concentrating the lateral force at the link center, rather than distributing it along the link, replaces (5) with $M_i = 0$ for each link, allowing free rotation. Second, in the limit that the lateral/longitudinal drag ratio approaches ∞ (from its value of 2 in (3) and (4)), these drag forces behave like the ideal nonholonomic constraints on the kinematic snake, preventing lateral motion while freely allowing longitudinal motion.

Likewise, the high Reynolds number swimmer bears a strong resemblance to the *three-link floating snake* [11, 14, 16], which consists of three links resting on a frictionless plane. In this case, the parallel is even easier to draw, as the floating snake is simply a high Reynolds number swimmer in which the added mass in (16) goes to zero, leaving only the actual inertias of the links. It may be of interest to note that while the high Reynolds number swimmer can both translate and rotate, the floating snake can only rotate; the directionality of the added mass allows the swimmer to “push off of” the surrounding fluid in a manner unavailable to the isolated floating system.

3 CONNECTION VECTOR FIELDS

The expressions for \mathbf{A} are somewhat complicated, and provide no particular insight as to the behavior of the system. Geometrically plotting them, however, does provide this insight and we have developed several tools for visualizing the local connection. The first of these tools is the *connection vector field* [16].

Each row of the local connection $\mathbf{A}(r)$ can be considered as defining a vector field $\vec{\mathbf{A}}^{\xi_i}$ on the shape space whose dot product with the shape velocity produces the corresponding component of the body velocity,

$$\xi_i = \vec{\mathbf{A}}^{\xi_i}(r) \cdot \dot{r} \quad (17)$$

where, for convenience, we wrap the negative sign into the vector field definition.⁶ These connection vector fields encode the (local) gradients of the position variables with respect to the shape variables, highlighting how the position changes in response to a given shape change: A shape change that follows a connection vector field moves the system positively along the corresponding body direction, while one that is orthogonal to the field produces no motion in the corresponding body direction.

⁶In strict differential geometric language, each row \mathbf{A}^i of \mathbf{A} is a one-form over M acting on \dot{r} , and $\vec{\mathbf{A}}^{\xi_i}$ is the negative dual of that one-form.

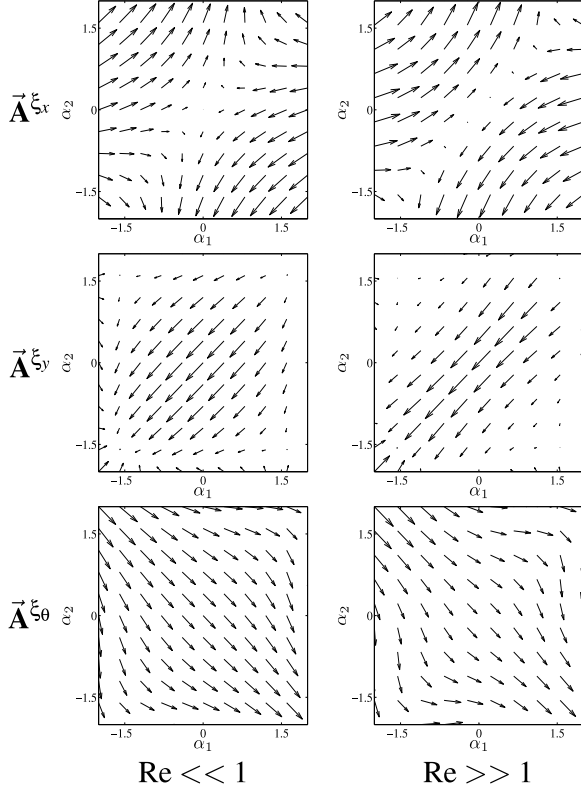


Figure 2: CONNECTION VECTOR FIELDS FOR THE LOW AND HIGH REYNOLDS NUMBER SWIMMERS.

The connection vector fields for the (hydrodynamically decoupled) swimming models described above are shown in Fig. 2, with an aspect ratio of $a/b = 10$ for the elliptical links of the high Reynolds number model. The strong resemblance between the two sets of fields is immediately apparent, and underscores the physical similarities between the two systems: while the fluid forces on the links are viscous at low Reynolds numbers and inertial at high Reynolds numbers, they both resist lateral motion significantly more strongly than they do longitudinal motion, forcing the swimmers into trajectories that minimize lateral motion of their links.

We can also build physical intuition for the systems by observing the individual structures of the fields. For instance, both \vec{A}^{ξ_θ} fields have a general heading in the $+\alpha_1, -\alpha_2$ direction. Returning to the geometry of the swimmer in Fig. 1(a), we see that this heading encodes a tendency for the center link to counterrotate with respect to the outer links. Physically, this makes sense, as rotating an outer link towards the center link generates opposite reaction forces on the center link. Similar intuition applies to other features of the vector fields, such as how the \vec{A}^{ξ_x} and \vec{A}^{ξ_y} fields approach zero magnitude in the vicinity of $\alpha = (0, 0)$ for \vec{A}^{ξ_x} and $\alpha = (\pm\pi/2, \pm\pi/2)$ for \vec{A}^{ξ_y} : In these shapes the outer links are respectively aligned or perpendicular to the center link, and lateral reaction forces on them project into pure lateral or pure longitudinal forces on the center link.

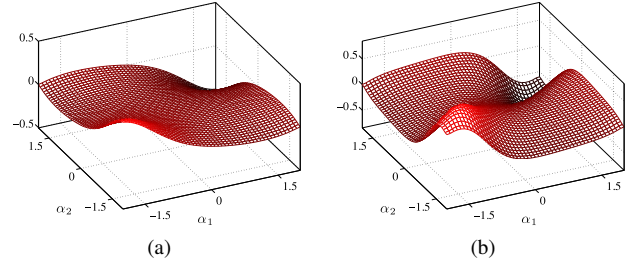


Figure 3: θ HEIGHT FUNCTIONS FOR THE (a) LOW AND (b) HIGH REYNOLDS NUMBER SWIMMERS.

4 CONNECTION HEIGHT FUNCTIONS

Connection vector fields illustrate the instantaneous relationship between shape and position changes, but do not directly convey information about the *net* change in position over a sequence of shape motions. Knowledge about the net motion produced by the systems plays a key part in understanding and controlling their behavior, as the joint limits force the systems to use cyclic motions that include both forward and backward segments. To this end, we employ curvature analysis, in the form of *connection height functions* [8, 9, 14].

By Green's form of Stokes's theorem [20], the line integral on a vector field along a closed loop is equal to the area integral of the field's curl over the interior of the loop. Plotting the curl of \vec{A}^{ξ_θ} as a height function on the shape space, as in Fig. 3, allows us to easily identify cyclic strokes that produce desired net rotations: For positive net rotation (positive value of $\Delta\theta = \int \xi_\theta$), the most effective strokes are those that positively (counterclockwise) encircle regions of the shape space where $\text{curl } \vec{A}^{\xi_\theta} > 0$ or negatively (clockwise) encircle regions where $\text{curl } \vec{A}^{\xi_\theta} < 0$. Conversely, when zero net rotations are desired (such as when the system should move in a straight line over repeated iterations of a stroke), the stroke should encircle regions from the second or fourth quadrants, or explicitly balance negative and positive regions in its encirclements.

Unfortunately, $\Delta x \neq \int \xi_x$ and $\Delta y \neq \int \xi_y$, and an exact height function formulation for the translation of the swimming systems does not exist. As explained in [8], the noncommutativity of the $SE(2)$ position space prevents such a formulation at a theoretical level; intuitively, stepping forward then turning results in a different translation from turning then stepping forward, and using Stokes's theorem discards the order of the steps. An approximate formulation incorporating Lie brackets has been suggested [8, 9], but is limited to infinitesimal, or in special cases, small finite, strokes. As an alternative to this formulation, we have developed an approach that uses an optimal choice of coordinates to largely remove the noncommutativity of the position space. This approach thus allows for the approximate application of the basic height functions to the swimmers' translation with a high degree of accuracy.

5 OPTIMIZED COORDINATES

The fundamental problem with integrating for translation on a connection vector field via Stokes’s theorem is that the resulting quantity, which we term the *body velocity integral*, or BVI [17], does not measure the net displacement; instead, it measures the “forwards minus backwards” motion in each body direction. Planar rotations always commute with each other and are unaffected by translations,⁷ so the rotational component of the BVI corresponds to the net rotation, as explained in §4. Translations specified in body coordinates only commute when there are no intervening rotations; for example, moving a system forward and backward by one unit each returns it to the origin, but interposing a rotation between the two steps leaves the system with a net translation, even though the net BVI over the motion is zero.

This lack of commutativity has previously been viewed as inherent to the locomoting systems [8]. In our work on nonholonomic systems, however, we observed that in many instances the noncommutativity can be alleviated by an appropriate choice of coordinates for the position g [17]. In these choices of coordinates, the reference line on the system used to represent its orientation θ rotates very little in response to changes in shape, allowing the translation motions produced by those shape changes to “almost commute.” More recently, we have systematically identified optimal choices of coordinates that minimize the difference between the BVI and the net displacement [18].

Optimizing the coordinates for both three link swimmers finds the best choices for g to be approximately the mean orientation of the three individual links and the center of mass location, with small, shape-dependent weightings of the contribution of each link to the averages. Figure 4 shows how these new coordinates affect our representation, with the swimmer shown in five shapes with orientation $\theta = 0$. Using the coordinates from Fig. 1(a), the center links of the swimmer are aligned across the different shapes, but in the new coordinates, the dotted lines representing the mean orientation are now aligned.

The connection vector fields and height functions for the two swimmers in the optimized coordinates are shown in Figs. 5(a) and 5(b). These plots highlight several interesting features of the coordinate optimization process and the differences between the motions of the low and high Reynolds number swimmers. First, the height functions for θ are unchanged in the new coordinates, even though their respective connection vector fields have clearly been modified. As explained in [18], θ is optimized by applying the Hodge-Helmholtz decomposition [21] to the original \vec{A}^{ξ_0} field to separate it into its gradient and rotational components; the gradient component encodes the relationship between the original and optimized measures of θ , and the rotational component is the new \vec{A}^{ξ_0} . As the gradient component of a vector field by definition does not contribute to its curl, removing it from \vec{A}^{ξ_0} does not modify the associated height function.

Second, symmetries in the motion of the swimmer are immediately apparent, suggesting locations for single-loop and

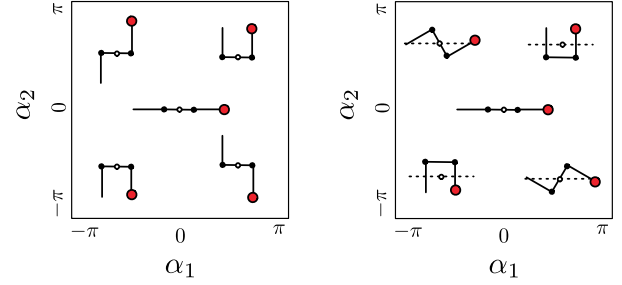


Figure 4: CONFIGURATION OF THE SWIMMER IN THE ORIGINAL AND OPTIMIZED COORDINATES.

figure-eight strokes that produce displacements in specific directions [14]. Third, the magnitudes of the connection vector fields and height functions are significantly larger for the high Reynolds number swimmer. Going back to the derivations in §2, we observe that the ratio of lateral to longitudinal drag on the low Reynolds number swimmer is 2 : 1, while the added masses at high Reynolds number are based on the 10 : 1 aspect ratio of the links; we hypothesize that the high Reynolds number swimmer is thus able to gain a greater difference from “pushing” links longitudinally and “pulling” them laterally than is the low Reynolds number system, and thus achieve greater velocities and displacements over comparable strokes.

6 ANALYSIS

Using the height functions in optimized coordinates, we can now start to answer some previously posed questions about swimming, and to explain prior result about optimal strokes that had been reached only by numerically integrating the swimmers’ motions over a wide array of candidate strokes.

6.1 Purcell’s Swimmer

The three-link swimmer was introduced by E. M. Purcell as an example in his lecture “Life at Low Reynolds Numbers” [2]. He also assigned to it the simplest possible stroke, in which the joints move individually and sweep through equal positive and negative angles, and used symmetry arguments to show that the stroke moves the swimmer forward. More recently, Becker *et al.* [22] expanded these results to show that a sufficiently large-amplitude Purcell stroke moves the swimmer *backward*. While their results explain this effect, they do not provide any insight as to the underlying mathematical structure. This structure is, however, captured by the height functions.

Purcell strokes trace out squares on the shape space, of the form shown in Fig. 6(a). At small amplitudes, the x height function is entirely negative in the region bounded by the square, so following the square clockwise produces a net positive displacement in the x direction (all the squares symmetrically enclose positive and negative regions of the y and θ height functions, so we focus our attention on the x direction). As the amplitudes grow larger, they first expand the negative region they enclose,

⁷This property is related to $SE(2)$ ’s structure as a *semi-direct product group*.

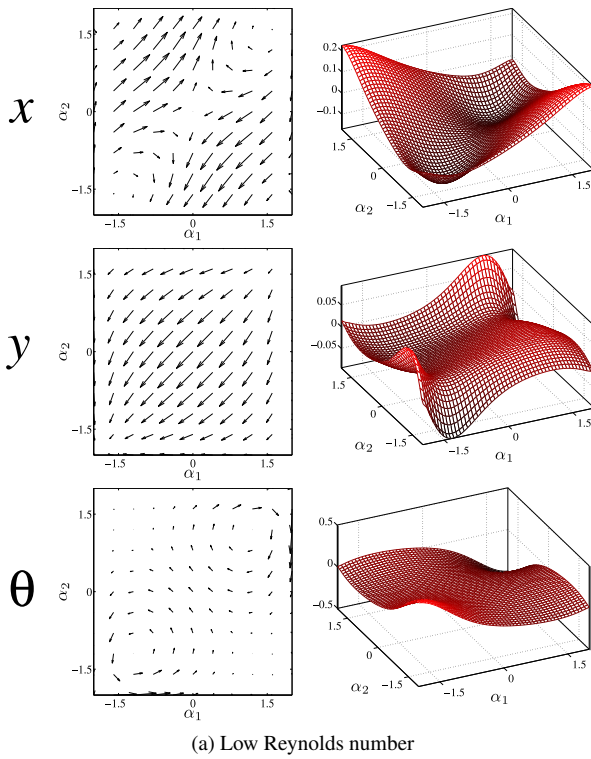
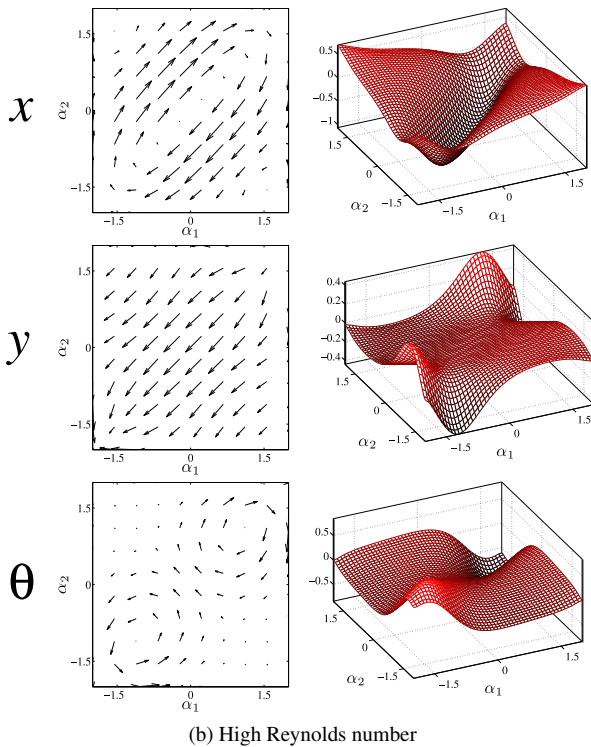


Figure 5: CONNECTION VECTOR FIELDS AND HEIGHT FUNCTIONS IN OPTIMIZED COORDINATES.



(b) High Reynolds number

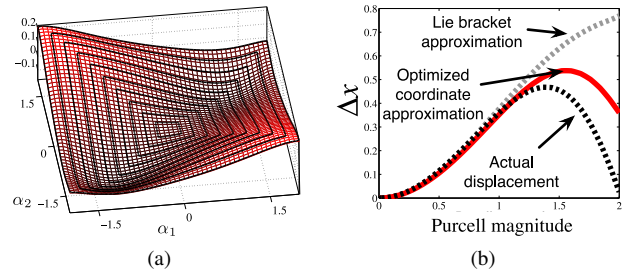


Figure 6: PURCELL STROKES AND RESULTING DISPLACEMENTS.

then start incorporating positive area, reducing the magnitude of displacement and eventually changing its sign. Figure 6(b) demonstrates that the BVI/displacement approximation on which this height function explanation rests is essentially exact for Purcell magnitudes up to 1 radian and continues to correctly reflect the trend at greater magnitudes. By contrast, the similar argument presented in [9] rests on the coarser approximation of applying Lie bracket operations to finite-scale motion. As shown in Fig. 6(b) the divergence between this approximation and the true displacement beyond the 1 radian point is much larger than with our new approximation.

6.2 Optimal Stroke at Low Reynolds Number

Recognizing that the square Purcell stroke is not the most efficient choice for locomotion, Tam and Hosoi [5] investigated optimal stroke patterns. Their basic finding was that optimal gaits tend to be rounded oblongs; this makes sense from our height function standpoint, as rounded curves have larger area-to-perimeter ratios than do curves with sharp angles, and the non-uniformity of the height functions can be expected to bias the optimal curves away from simple circles. A second, more striking, result was that the speed-optimal stroke (maximizing net-distance traveled over time when executed at its most efficient pace) is pinched in at the center, rather than being convex. This “peanut” shape, plotted on the \vec{A}^{ξ_x} field in Fig. 7(a) bears a striking resemblance to the contours of the height function in the x direction, shown in Fig. 7(b), pointing to the pinched shape as a balance between maximizing the area-to-perimeter ratio while avoiding areas of positive curl that decrease the net displacement gained over the gait.

6.3 Optimal Stroke at High Reynolds Number

Kanso [6] used a similar direct integration approach to find optimal gaits for the high Reynolds number swimmer. While the set of candidate gaits was restricted to simple ellipses, limiting our ability to comment here on any commonalities between the optimal stroke and height function contours, the ellipses in that work are aligned with the well in the x height function for the high Reynolds number system in Fig. 5(b), further confirming the height functions’ qualities as predictors of good strokes.

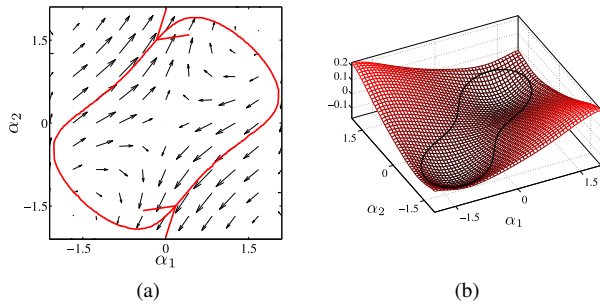


Figure 7: LOW REYNOLDS NUMBER SWIMMER OPTIMAL STROKE AND HEIGHT FUNCTION CONTOUR.

7 CONCLUSIONS

In this paper, we present a novel perspective for modeling articulated swimmers, which in turn improves upon existing methods for prescribing strokes. The connection vector fields, which we originally developed for mechanical systems, provide a concise visualization of the swimmers' dynamics. They naturally induce the connection height functions, which geometrically capture the effect of oscillatory strokes. Our coordinate optimization approach makes these height functions significantly more accurate than similar height functions considered by others in the swimming community, especially when analyzing large-amplitude (and hence generally more efficient) strokes.

Building off of these observations, our future work will examine the feasibility of using the height functions to identify good regions of the stroke-function space in which to look for optimal strokes. We will also generate connection vector fields and height functions for the hydrodynamically coupled swimming models, for comparison with the first-order models. Finally, we will continue to develop the theoretical underpinnings of the optimal coordinate formulation, including whether there are systems for which combining it with the Lie bracket approach is beneficial.

We would like to thank Anette Hosoi, Lisa Burton, and Scott Kelly for their insightful discussions.

REFERENCES

- [1] Taylor, G., 1951. "Analysis of the Swimming of Microscopic Organisms". *Proceedings of the Royal Society of London. Series A, Mathematical and Physical Sciences*, **209**(29), pp. 447–461.
- [2] Purcell, E. M., 1977. "Life at Low Reynolds Numbers". *American Journal of Physics*, **45**(1), January, pp. 3–11.
- [3] Lauder, G. V., and Madden, P. G. A., 2007. "Fish Locomotion: Kinematics and Hydrodynamics of Flexible Foil-like Fins". *Experiments in Fluids*, **43**, July, p. 641:653.
- [4] Kelly, S. D. The Mechanics and Control of Driftless Swimming. In press.
- [5] Tam, D., and Hosoi, A. E., 2007. "Optimal Stroke Patterns for Purcell's Three-Link Swimmer". *Phys. Review Letters*, **98**(6), pp. 068105 (1–4).
- [6] Kanso, E., 2009. "Swimming Due to Transverse Shape Deformations". *Journal of Fluid Mechanics*, **631**, pp. 127–148.
- [7] Morgansen, K., Triplett, B., and Klein, D., 2007. "Geometric Methods for Modeling and Control of Free-Swimming Fin-Actuated Underwater Vehicles". *IEEE Transactions on Robotics*, **23**(6), Jan, pp. 1184–1199.
- [8] Melli, J. B., Rowley, C. W., and Rufat, D. S., 2006. "Motion Planning for an Articulated Body in a Perfect Planar Fluid". *SIAM Journal of Applied Dynamical Systems*, **5**(4), November, pp. 650–669.
- [9] Avron, J., and Raz, O., 2008. "A Geometric Theory of Swimming: Purcell's Swimmer and its Symmetrized Cousin". *New Journal of Physics*, **9**(437).
- [10] Murray, R., and Sastry, S., 1993. "Nonholonomic Motion Planning: Steering Using Sinusoids". *IEEE Transactions on Automatic Control*, **38**(5), Jan, pp. 700–716.
- [11] Kelly, S., and Murray, R. M., 1995. "Geometric Phases and Robotic Locomotion". *J. Robotic Systems*, **12**(6), Jan, pp. 417–431.
- [12] A. M. Bloch *et al.*, 2003. *Nonholonomic Mechanics and Control*. Springer.
- [13] Ostrowski, J., and Burdick, J., 1998. "The Mechanics and Control of Undulatory Locomotion". *International Journal of Robotics Research*, **17**(7), July, pp. 683 – 701.
- [14] Shammas, E. A., Choset, H., and Rizzi, A. A., 2007. "Geometric Motion Planning Analysis for Two Classes of Underactuated Mechanical Systems". *The International Journal of Robotics Research*, **26**(10), pp. 1043–1073.
- [15] Shapere, A., and Wilczek, F., 1989. "Geometry of Self-Propulsion at Low Reynolds Number". *Journal of Fluid Mechanics*, **198**, pp. 557–585.
- [16] Hatton, R. L., and Choset, H., 2008. "Connection Vector Fields for Underactuated Systems". In Proceedings of the IEEE BioRobotics Conference, pp. 451–456.
- [17] Hatton, R. L., and Choset, H., 2009. "Approximating Displacement with the Body Velocity Integral". In Proceedings of Robotics: Science and Systems.
- [18] Hatton, R. L., and Choset, H., 2010. "Optimizing Coordinate Choice for Locomoting Systems". In Proceedings of IEEE International Conference on Robotics and Automation (accepted).
- [19] Cox, R. G., 1970. "The Motion of Long Slender Bodies in a Viscous Fluid Part I. General Theory". *Journal of Fluid Mechanics*, **44**(4), pp. 791–810.
- [20] Boothby, W. M., 1986. *An Introduction to Differentiable Manifolds and Riemannian Geometry*. Academic Press.
- [21] Arfken, G. B., 2005. *Mathematical Methods for Physicists*, 6th ed. Elsevier.
- [22] Becker, L., Koehler, S. A., and Stone, H. A., 2003. "On Self-propulsion of Micro-machines at Low Reynolds Number: Purcell's three-link swimmer". *Journal of Fluid Mechanics*, **490**, pp. 15–35.